

# Aeration and air–water mass transfer on stepped chutes with embankment dam slopes

Stefan Felder · Hubert Chanson

Received: 24 April 2014 / Accepted: 22 July 2014 / Published online: 6 August 2014  
© Springer Science+Business Media Dordrecht 2014

**Abstract** Stepped spillway flows are characterised by significant free-surface aeration downstream of the inception point of air entrainment. The stepped design is advantageous for applications which require large energy dissipation and strong flow aeration. While the energy dissipation rate for embankment stepped spillways was studied previously, the optimum design for aeration and air–water mass transfer is not known. Herein new air–water flow experiments were conducted on several stepped spillways with embankment dam slopes using with phase-detection intrusive probes. The present data were compared with previous studies in terms of energy dissipation, flow aeration and air–water mass transfer. The air–water mass transfer was calculated based upon air–water flow measurements in terms of dissolved oxygen. The re-oxygenation rates were compared with previous studies comprising both conductivity and direct dissolved oxygen measurements. The comparison highlighted a monotonic increase of aeration efficiency with energy dissipation rate. All data were in good agreement independent of channel slopes, stepped configuration and sensor size. The data confirmed the effects of strong air–water interactions within the bulk of the flow for both energy dissipation and re-oxygenation performances.

**Keywords** Stepped spillway · Aeration · Air–water mass transfer · Air–water flow properties · Energy dissipation · Optimum design

## 1 Introduction

A key characteristic of self-aerated stepped spillway flows is the significant aeration downstream of the inception point of air entrainment. At the upstream end, the flow appears glassy

---

S. Felder (✉)  
Water Research Laboratory, School of Civil and Environmental Engineering,  
The University of New South Wales, Manly Vale, NSW 2093, Australia  
e-mail: s.felder@unsw.edu.au

H. Chanson · S. Felder  
School of Civil Engineering, The University of Queensland, Brisbane, QLD 4072, Australia  
e-mail: h.chanson@uq.edu.au



**Fig. 1** Air–water flows on a stepped spillway ( $\theta = 26.6^\circ$ ) with flat steps; Free-surface aeration downstream of the inception point for a skimming flow regime ( $d_c/h = 1.37$ ,  $q_w = 0.159 \text{ m}^2/\text{s}$ ,  $Re = 6.3 \times 10^5$ )

and a boundary layer starts to develop at the boundary of the broad-crested weir. The boundary layer grows along the stepped section and when the turbulence fluctuations next to the free-surface are large enough, the air entrainment process starts naturally at the inception point of free-surface aeration. Immediately downstream of the inception point, the flow rapidly varies and the air content increases over a small distance (Fig. 1). Further downstream of the inception point, the flow becomes gradually varied and a highly turbulent air–water flow mixture exists which enables a sustained entrainment of air. The air–water flows are highly complex and strong energetic interactions between air bubbles and water droplets take place. At some distance downstream of the inception point, uniform equilibrium flow condition might be reached when characteristic air–water flow properties do not change in downstream flow direction. It was argued by [9] that no equilibrium flow conditions existed on stepped spillways and the experiments of [1] and [14] indicated characteristic seesaw patterns in the skimming flow regime.

The strong aeration is a key characteristic of stepped spillway flows which is relevant to re-oxygenation applications such as in waste water treatment, chemical applications or for rivers under environmental stresses. Hence the quantification of the aeration performance and air–water mass transfer rate is an important design parameter. Recently [3,29] quantified the re-oxygenation with direct dissolved oxygen measurements on the downstream end of stepped spillways with slopes of  $\theta = 3.4^\circ$ ,  $18.4^\circ$  and  $26.6^\circ$ . Further researchers studied the air entrainment performances on stepped spillways with embankment dam slopes  $3.4^\circ \leq \theta \leq 26.6^\circ$  (e.g. [2, 11, 12, 14–16, 19, 25]) using phase-detection intrusive probes. Herein detailed air–water flow measurements with phase-detection intrusive probes were conducted on stepped chutes with flat, pooled and porous pooled steps with  $\theta = 8.9^\circ$  and  $26.6^\circ$  and the data were analysed in terms of flow aeration, energy dissipation and re-oxygenation rate.

Phase-detection intrusive probes can measure characteristic air–water flow properties including void fraction, bubble count rate and interfacial velocity and further characteristic aeration parameters including the mean air concentration  $C_{\text{mean}}$ :

$$C_{\text{mean}} = \frac{1}{Y_{90}} \times \int_0^{Y_{90}} C \times dy \tag{1}$$

where  $Y_{90}$  is the characteristic flow depth where  $C = 0.9$ . The mean air concentration  $C_{\text{mean}}$  is the depth averaged characteristic void fraction parameter describing the aeration within a cross-section.

The air–water mass transfer between two interfaces is stated in Fick’s Law, which expresses the mass transfer rate as function of the diffusion coefficient and of the gradient of gas concentration. In stepped spillway flows, the air–water mass transfer is proportional to the air–water interface area and the concentration gradient between air and water. The air phase in water consists of a volatile liquid (e.g. oxygen) and the mass transfer equation can be expressed as [7,28,29]:

$$\frac{\partial}{\partial t} C_{\text{gas}} = k_L \times a \times (C_{\text{sat}} - C_{\text{gas}}) \tag{2}$$

where  $C_{\text{gas}}$  is the local concentration of the dissolved gas,  $C_{\text{sat}}$  is the concentration of dissolved gas in water at equilibrium (herein  $C_{\text{sat}} = 9.2$  mg/l for  $O_2$ ) [21],  $k_L$  is the liquid film coefficient and  $a$  is the specific interfacial area. The liquid film coefficient is a factor for the mass transfer and almost constant for all bubble chord sizes and flow conditions [22]:

$$k_L = 0.47 \times \sqrt{D_{\text{gas}}} \times \left( \frac{\mu_w}{\rho_w} \right)^{-1/6} \times \sqrt[3]{g} \tag{3}$$

where  $\mu_w$  and  $\rho_w$  are the dynamic viscosity and density of water respectively and  $D_{\text{gas}}$  is the molecular diffusivity for oxygen [18]:

$$D_{\text{gas}} = 1.16793 \times 10^{-27} \times T_K^{7.3892} \quad (\text{for } O_2) \tag{4}$$

The molecular diffusivity for oxygen was calculated for a temperature in Kelvin  $T_K = 293$  K (i.e. 20 Celsius).

Equation (2) may be transformed to account for the mass transfer between successive cross-sections:

$$\frac{\partial}{\partial x} C_{\text{gas}} = \frac{k_L \times a_{\text{mean}}}{U_w} (C_{\text{sat}} - C_{\text{gas}}) \tag{5}$$

where  $x$  is the longitudinal distance along the stepped chute,  $U_w$  the mean flow velocity and  $a_{\text{mean}}$  the depth-averaged specific interfacial area measured with a conductivity probe:

$$a_{\text{mean}} = \frac{1}{Y_{90}} \times \int_0^{Y_{90}} a \times dy \tag{6}$$

where the specific interface area for any bubble shape and chord size distribution can be estimated as [6]:

$$a = \frac{4 \times F}{V} \tag{7}$$

The interface area is proportional to the number of entrained air bubbles  $F$  and inversely proportional to the interfacial velocity  $V$ . The aeration efficiency was therefore enhanced in presence of large numbers of small entrained air bubbles and slow flow velocities.

In stepped spillway flows, the overall gas transfer may be quantified by integrating Equation (5) along the stepped chute from the inception point of air entrainment until the downstream end. The aeration efficiency in terms of oxygen  $E(O_2)$  can then be expressed as [28,29]:

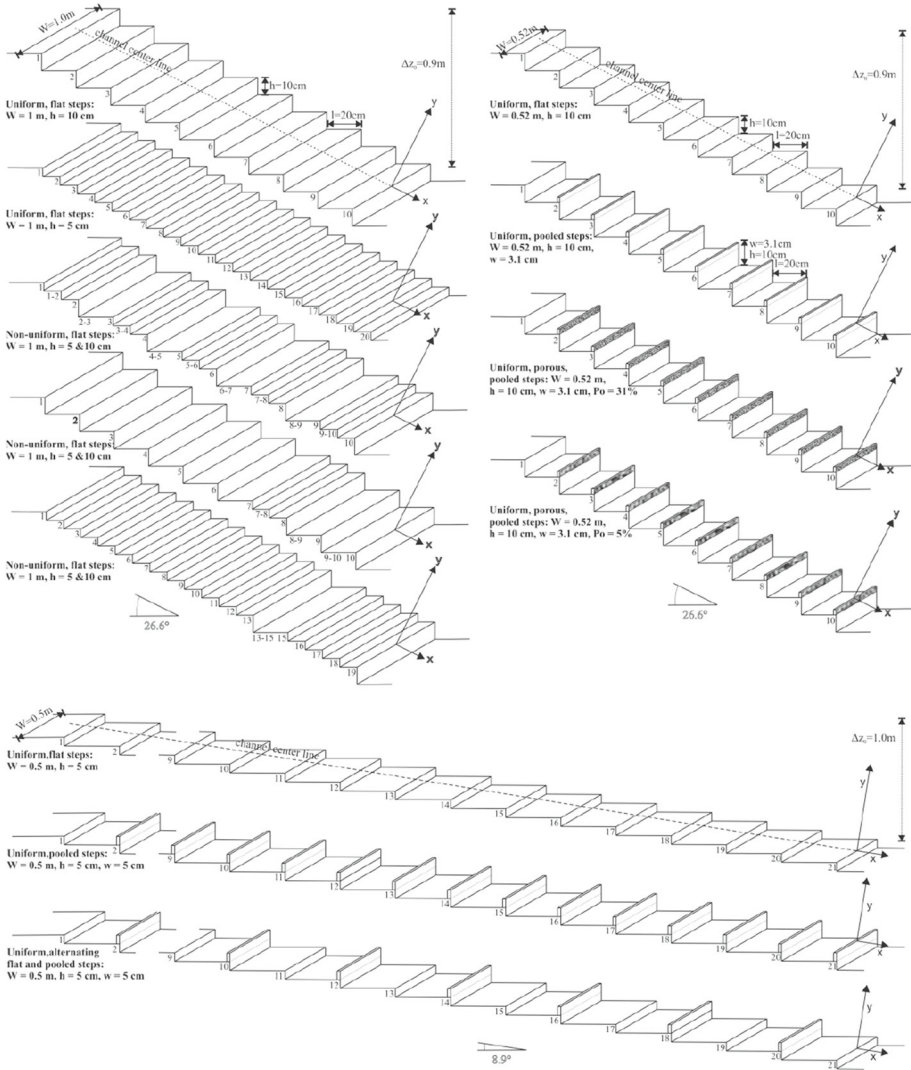


**Fig. 2** Experimental configurations in the present study comprising flat uniform, flat non-uniform, pooled and porous pooled steps;  $\theta = 8.9^\circ$  and  $26.6^\circ$

$$E(O_2) = 1 - \frac{C_{\text{sat}} - (C_{\text{gas}})_{d/s}}{C_{\text{sat}} - (C_{\text{gas}})_{u/s}} C_{\text{gas}} = \frac{(C_{\text{gas}})_{d/s} - (C_{\text{gas}})_{u/s}}{C_{\text{sat}} - (C_{\text{gas}})_{u/s}} \quad (8)$$

where  $(C_{\text{gas}})_{u/s}$  is the upstream dissolved gas concentration and  $(C_{\text{gas}})_{d/s}$  the dissolved gas concentration at the downstream end of the stepped chute.

## 2 Instrumentation and experimental program

In high-velocity air–water flows, the use of classical mono-phase flow instrumentation is not possible due to the three dimensional air–water flow with large amounts of air–water

interfaces (Fig. 1). Phase-detection intrusive probes are commonly used, and experimental studies with optical fibre probes (e.g. [1]) and conductivity probes (e.g. [2, 10, 13, 28]) were successfully conducted in stepped spillways. In the present study, conductivity probes were used (Table 1). The principle of the conductivity probe is based upon the different resistivity of air and water providing an instantaneous voltage signal. The signal of a single sensor may be analysed with a threshold technique to calculate the time averaged local air concentration or void fraction  $C$ , the number of air-to-water (or water-to-air) voltage changes expressed as bubble count rate  $F$  and the air bubble and water droplet chord sizes. For a double-tip conductivity probe with longitudinal separation between the two probe sensors, the cross-correlation analysis of the signals leads to the local time-averaged interfacial velocity  $V$ . Details about the signal processing techniques can be found in [8] and [13].

The present experiments were conducted on several stepped spillways with slopes of  $\theta = 8.9^\circ$  and  $26.6^\circ$  comprising flat uniform, flat non-uniform, pooled steps and porous pooled steps with step height  $h = 5$  cm and  $5$  cm respectively (Fig. 2). The experimental facilities were large scale to minimize viscous scale effects affecting the microscopic air–water flow processes in high-velocity free-surface flows [15]. For all stepped configurations, air–water flow experiments were performed with conductivity phase-detection intrusive probes at all step edges downstream of the inception point of air entrainment. The double-tip conductivity probes had sensor sizes of  $\varnothing = 0.13$  mm and  $0.25$  mm and were sampled for a duration of  $45$  s with a frequency of  $20$  kHz per sensor. The discharges comprised transition and skimming flow rates  $0.035 \leq q_w \leq 0.234$  m<sup>2</sup>/s for the spillways with  $\theta = 8.9^\circ$  and  $0.02 \leq q_w \leq 0.249$  m<sup>2</sup>/s for  $\theta = 26.6^\circ$  comprising Reynolds numbers of  $1.4 \times 10^5 \leq Re \leq 9.3 \times 10^5$  and  $8.1 \times 10^4 \leq Re \leq 9.9 \times 10^5$  respectively (Table 1).

The present experimental conditions are summarised in Table 1 comprising the channel slope, the step height  $h$ , the channel width  $W$ , the flow rate per unit width  $q_w$ , the dimensionless flow rate  $d_c/h$  with  $d_c$  the critical flow depth, the conductivity probe and sampling specifics and further relevant information about the design. Table 1 lists also the details of further experimental studies of air–water flows on stepped spillways with embankment dam slopes. Two studies measured the aeration efficiency based upon dissolved oxygen ([3, 29]) while the other studies measured the air–water flow properties with conductivity probes. For completeness, the data in Table 1 include also one air–water data set for a smooth spillway [5]. All experimental studies comprised typical embankment dam slopes and important information about the aeration and air–water mass transfer on stepped spillways. Herein the mean air concentration  $C_{\text{mean}}$ , the maximum bubble count rate  $F_{\text{max}}$  and the aeration efficiency  $E(\text{O}_2)$  were compared for the embankment dam slopes to identify optimum aeration performances.

### 3 Air–water flow properties and energy dissipation

For all stepped configurations, the air–water flow properties were measured downstream of the inception point of free-surface aeration. Typical distributions are illustrated in Fig. 3 including the void fraction, the bubble count rate, the interfacial velocity and the interfacial area as function of the dimensionless distance perpendicular to the step edge  $y/Y_{90}$ . The present observations were consistent with previous experimental air–water flow studies (e.g. [2, 10, 13, 28]).

For all data sets, the void fraction distributions compared well with an analytical solution of the advective diffusion equation for air bubbles [11]:

**Table 1** Experimental configurations of aeration and air–water mass transfer experiments on the present and further stepped spillways with flat steps ( $3.4^\circ \leq \theta \leq 26.6^\circ$ )

Reference	Slope ( $^\circ$ )	W (m)	h (cm)	$q_w$ ( $m^2/s$ )	$d_c/h$ (–)	Conductivity probe	Sampling rate/duration	Comment
[29]	3.4	0.5	14.3	0.08–0.15	0.61–0.92	N/A	N/A	10 steps, ( $L=25$ m); Dissolved oxygen measurements
[3]	18.4 and 26.6	0.3	3 & 6	0.07–0.11	2.65–3.58	N/A	N/A	$H_{dam}=2.4$ m; Dissolved oxygen measurements
[5]	4.0	0.5	N/A	0.142–0.164	N/A	Double-tip ( $\varnothing=0.025$ mm)	40 kHz / 5.12 s	Smooth chute ( $L=25$ m) for comparison
[12]	3.4	0.5	7.15 and 14.3	0.08–0.15	0.61–1.85	Single-tip ( $\varnothing=0.35$ mm)	5 kHz/60 and 180 s	10 and 18 steps, ( $L=25$ m)
[25]	5.7 and 11.3	0.4	0.63–5.0	0.02–0.08	1.25–14.3	Single-tip ( $\varnothing=0.1$ mm)	2 kHz/60 s	$H_{dam}$ between 30 and 70 cm
[27]	14.6	0.5	5 and 10	0.05–0.234	1.27–3.55	Double-tip ( $\varnothing=0.13$ mm)	30 kHz/40 s	26 steps
[11]	15.9 and 21.8	1.0	10	0.069–0.188	0.78–1.53	Double-tip ( $\varnothing=0.025$ mm)	20 kHz / 20 s	9 steps
[19]	15.9	1.0	5 and 10	0.021–0.220	0.6–3.2	Double-tip ( $\varnothing=0.025$ mm)	20 kHz/20 s	9 and 18 steps
[2]	18.4 and 26.6	0.3	3 and 6	0.07–0.11	2.65–3.58	Double-tip ( $\varnothing=0.13$ mm)	25 kHz/25 s	$H_{dam}=2.4$ m
[19]	21.8	1.0	10	0.114–0.220	1.1–1.7	Double-tip ( $\varnothing=0.025$ mm)	20 kHz/20 s	10 steps

**Table 1** continued

Reference	Slope (°)	W (m)	h (cm)	$q_w$ (m <sup>2</sup> /s)	$d_c/h$ (-)	Conductivity probe	Sampling rate/duration	Comment
[4]	21.8	1.0	10	0.095–0.180	1.0–1.57	Double-tip ( $\varnothing=0.25$ mm)	20 kHz/45 s	10 steps
[14]	21.8	1.0	5	0.059–0.158	1.17–3.16	Double-tip ( $\varnothing=0.25$ mm)	20 kHz/45 s	20 steps
[20]	26.6	0.52	10	0.03–0.217	0.5–1.7	Double-tip ( $\varnothing=0.25$ mm)	20 kHz/45 s	10 steps; in-line and staggered configurations of flat and pooled steps
Present study	8.9	0.5	5	0.035–0.234	1.0–3.55	Double-tip ( $\varnothing=0.13$ mm)	20 kHz/45 s	21 steps; flat and pooled step configurations
	26.6	1.0	5 and 10	0.020–0.227	0.69–3.30	Double-tip ( $\varnothing=0.25$ mm)	20 kHz/45 s	10 and 20 steps; flat and non-uniform step configurations
	26.6	0.52	10	0.073–0.249	0.82–1.85	Double-tip ( $\varnothing=0.25$ mm)	20 kHz/45 s	10 steps; flat and pooled step configurations

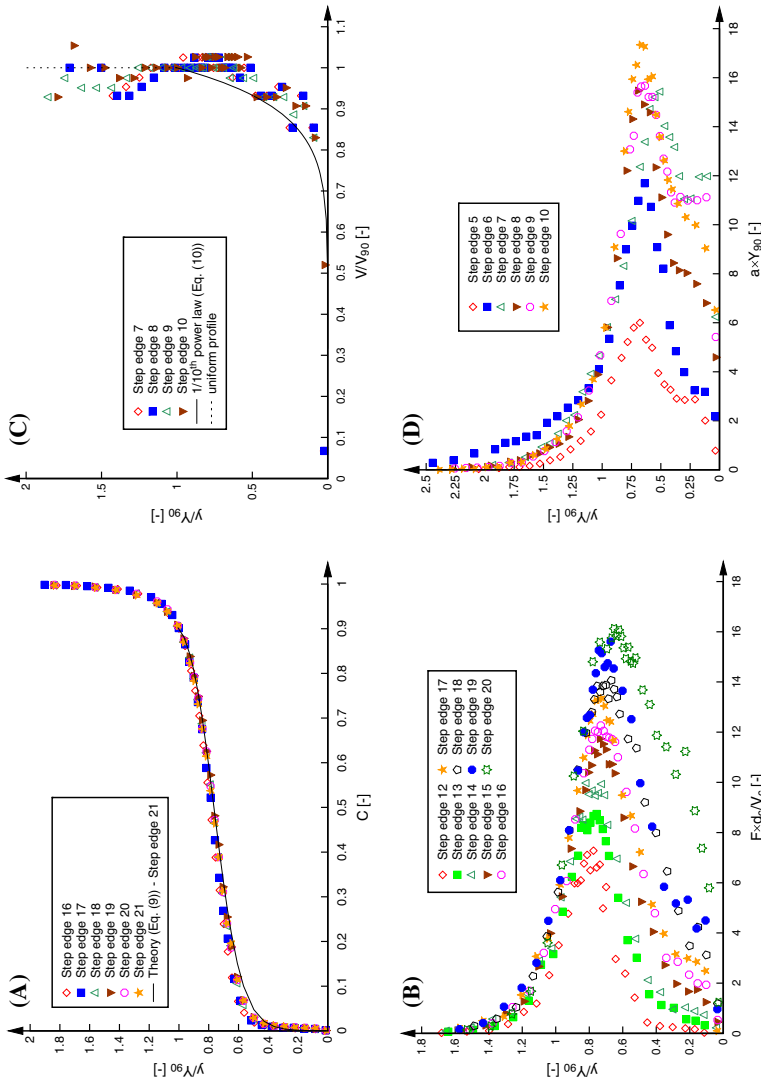


**Fig. 3** Air–water flow properties on flat stepped spillways downstream of the inception point of air entrainment. **a** Void fraction distributions and advective diffusion equation (Eq. 9):  $\theta = 8.9^\circ$ ,  $h = 5$  cm,  $d_c/h = 2.66$ ,  $q_w = 0.152$  m<sup>2</sup>/s,  $Re = 6.0 \times 10^5$ . **b** Bubble count rate distributions:  $\theta = 26.6^\circ$ ,  $h = 5$  cm,  $d_c/h = 2.66$ ,  $q_w = 0.116$  m<sup>2</sup>/s,  $Re = 4.6 \times 10^5$ . **c** Interfacial velocity distributions and power law correlation (Eq. 10):  $\theta = 26.6^\circ$ ,  $h = 10$  cm,  $d_c/h = 1.38$ ,  $q_w = 0.161$  m<sup>2</sup>/s,  $Re = 6.4 \times 10^5$ . **d** Interfacial area distributions:  $\theta = 26.6^\circ$ ,  $h = 10$  cm,  $d_c/h = 0.96$ ,  $q_w = 0.093$  m<sup>2</sup>/s,  $Re = 3.7 \times 10^5$

$$C = 1 - \tanh^2 \left( K' - \frac{y/Y_{90}}{2 \times D_o} + \frac{(y/Y_{90} - 1/3)^3}{3 \times D_o} \right) \tag{9}$$

where  $K'$  is an integration constant and  $D_o$  is a function of the mean air concentration  $C_{\text{mean}}$  only (Fig. 3a). The mean air concentration increased sharply downstream of the inception point and varied gradually with increasing distance downstream of the inception point. Similarly the number of entrained air bubbles increased immediately downstream of the inception point (Fig. 3b). With increasing distance in downstream direction, the number of air bubbles increased and no uniform equilibrium flow conditions were reached before the end of the stepped chute. This feature is visible in Fig. 3b where the bubble count rate is presented in dimensionless terms  $F \times d_c/V_c$  with  $V_c$  the critical flow velocity.

Typical dimensionless interfacial velocity  $V/V_{90}$  distributions are illustrated in Fig. 3c for several step edges with  $V_{90}$  the velocity where  $C = 0.9$ . The velocity distributions compared well with a power law with exponent 1/10:

$$\frac{V}{V_{90}} = \left( \frac{y}{Y_{90}} \right)^{1/N} \quad 0 \leq y/Y_{90} \leq 1 \tag{10}$$

For  $y/Y_{90} > 1$ , the data exhibited a uniform profile (Fig. 3c).

The dimensionless interfacial area distributions  $a \times Y_{90}$  showed a similar shape compared to the bubble count rate distributions with maxima in the intermediate flow region for  $C = 0.45$  to 0.6 (Fig. 3d). With increasing distance downstream of the inception point, the interfacial areas increased and no uniform equilibrium might exist at the downstream end of the stepped spillway test section.

For all present stepped configurations, the rate of energy dissipation was calculated at the last step edge based upon the upstream total head  $H = H_{\text{dam}} + 3/2 d_c$  and the residual energy  $H_{\text{res}}$  at the downstream end:

$$H_{\text{res}} = d \times \cos \theta + \frac{U_w^2}{2 \times g} + w = \int_{y=0}^{Y_{90}} (1 - C) dy \times \cos \theta + \frac{q_w^2}{2 \times g \times \left( \int_{y=0}^{Y_{90}} (1 - C) \times dy \right)^2} + w \tag{11}$$

where  $g$  is the gravity acceleration constant and  $w$  the pooled weir height for the pooled stepped spillway configurations. The total head loss along the chute was  $\Delta H = H_{\text{max}} - H_{\text{res}}$ . The energy dissipation data of the present study are illustrated in dimensionless terms  $\Delta H/H_{\text{max}}$  as a function of the dimensionless drop in elevation from the upstream end until the measured step edge  $\Delta z_o/d_c$  (Fig. 4). In Fig. 4, the present data are illustrated with colored symbols and compared with further reanalysed data from previous studies (Table 1). For all data sets, the energy dissipation rate was significant and large amounts of energy were dissipated in particular for the smaller flow rates. The rate of energy dissipation decreased with increasing discharge (Fig. 4). For certain large flow rates and above, the stepped chute flow becomes non-aerated and the energy dissipation capacity drops drastically [7,24]. In Fig. 4, this is visible in the sharp drop of the energy dissipation rate for the largest flow rates which were characterised by a smaller aerated distance between inception point and measurement position at the downstream end.

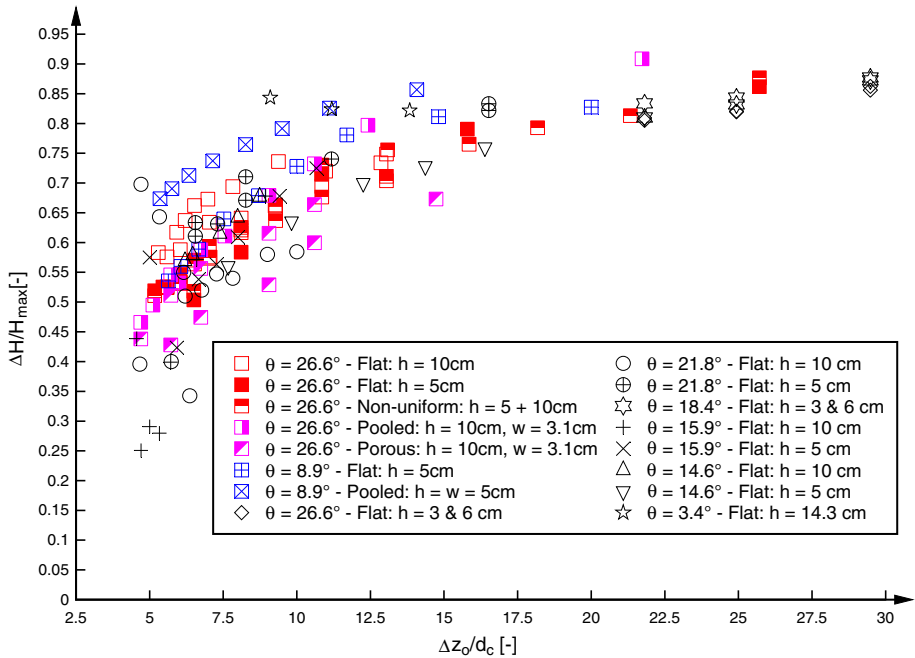


**Fig. 4** Energy dissipation rate on stepped spillways with embankment dam slopes ( $3.4^\circ \leq \theta \leq 26.6^\circ$ ); comparison of present data (coloured symbols) with previous data (Table 1, black symbols)

#### 4 Aeration performance

A characteristic parameter of the flow aeration is the mean air concentration  $C_{\text{mean}}$  which describes the depth-averaged air content. The mean air concentration for the flat and pooled step configurations in the present study were compared with further flat stepped spillways with embankment dam slopes at the downstream end of the stepped chutes (Fig. 5). The data were presented as a function of the channel slope to investigate the effect of the slope upon the aeration. In Fig. 5, the mean air concentration for the skimming flow discharges are compared with aeration data from a smooth spillway with  $\theta = 4^\circ$ , with the uniform equilibrium data of [26] on a smooth spillway with various channel slopes and with an equilibrium air concentration  $C_e = 0.9 \times \sin \theta$ .

While the aeration on the smooth spillway compared well with the equilibrium aeration [30], the mean air concentration for the stepped spillway data did not reach equilibrium air concentration. The experimental data exceeded the equilibrium aeration level for stepped spillways with  $\theta \leq 21.8^\circ$  with the largest differences for the smallest channel slopes. The mean air concentration was largest for the flat stepped spillways with  $\theta = 21.8^\circ$ . Interestingly, the mean air concentration was significantly smaller for the flat and pooled stepped spillways with  $\theta = 26.6^\circ$ . Within the range of typical embankment dam slopes ( $3.4^\circ \leq \theta \leq 26.6^\circ$ ), a stepped spillway with  $\theta = 21.8^\circ$  is optimum to maximize the air concentration. However, for larger channel slopes, experiments by [1] and [23] showed mean air concentrations  $C_{\text{mean}} > 0.6$  on stepped chutes with  $\theta \approx 50^\circ$ . Figure 5 compared solely skimming flow data and the aeration within the nappe and transition flow regimes were larger for all stepped spillways.

A further characteristic parameter for the quantification of the air entrainment performance is the maximum number of entrained air bubbles per unit time  $F_{\text{max}}$ . In all present stepped

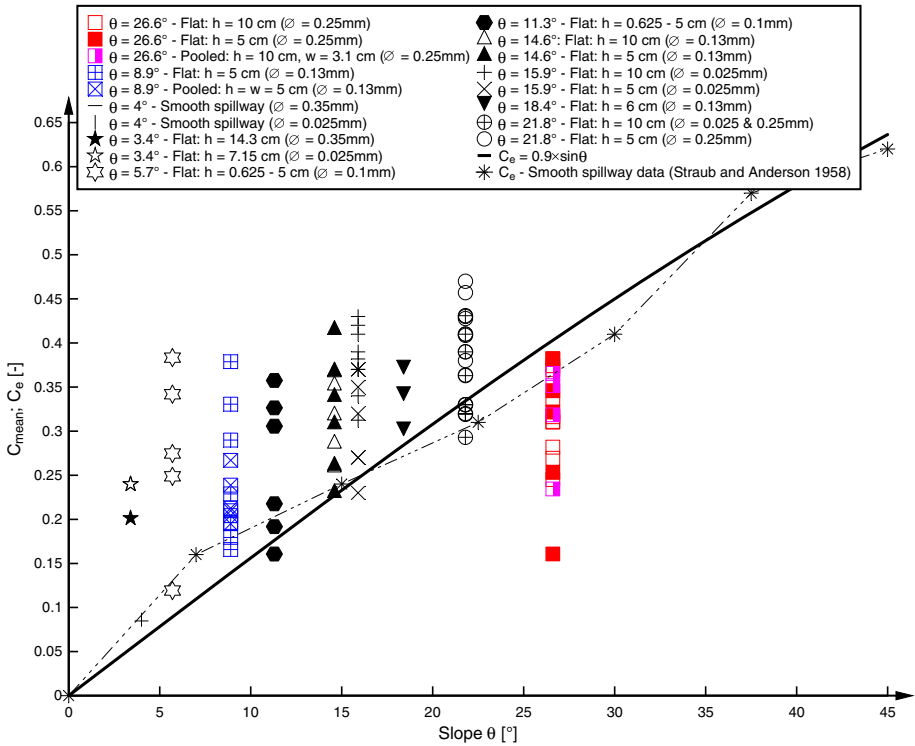


**Fig. 5** Depth-averaged air concentration at the downstream end on stepped spillways with embankment dam slopes ( $3.4^\circ \leq \theta \leq 26.6^\circ$ ) in skimming flows; comparison of present data (coloured symbols) with previous data (Table 1, black symbols) and the equilibrium air concentration on flat smooth chutes; Note the different conductivity probe sensor sizes

configurations, the maximum bubble count rate was observed in the intermediate flow region for air concentrations of about  $0.4 < C < 0.6$  as previously reported by [11]. The intermediate flow region was characterised by strong air bubble and water droplet interactions which were affected by free-surface waves [13]. Very energetic processes took place in this region and the largest turbulent levels and the largest integral turbulent scales were observed. The comparison of the present data with further studies (Table 1) is illustrated in Fig. 6 in terms of the maximum number of entrained air bubbles at the downstream end as a function of the chute slope. For all stepped spillways, significant bubble count rates were observed even though the flattest stepped chute slope indicated a smaller number of entrained bubbles ( $\theta = 3.4^\circ$ ). The largest maxima in bubble count rate were observed for stepped spillways with  $\theta = 15.9^\circ$  and  $21.8^\circ$  within the range of embankment dam slopes ( $3.4^\circ \leq \theta \leq 26.6^\circ$ ). However, it must be noted, that the sensor tip size was smallest for some of these experiments which led to a larger bubble count rate. As discussed by [4], the size of the conductivity probe tip affects the size of the smallest detectable air bubble and hence the total number of detected bubbles increases with decreasing tip size. Figure 6 illustrates maximum bubble count rates for different probe sensor sizes and the effects of sensor size were not investigated in detail. Furthermore, the length of the air–water flow region downstream of the inception point affects the bubble count rate since no uniform equilibrium flow is achieved at the downstream end of the stepped chute. The bubble count rate was affected by scale effects [15] and the comparison of the maximum number of entrained air bubbles might be underestimated for smaller step heights.

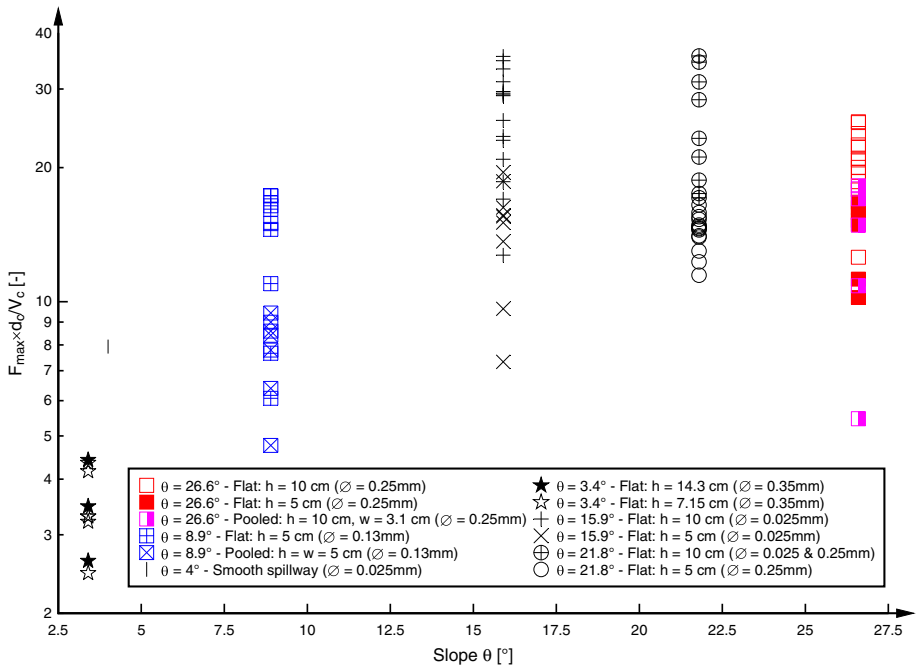


**Fig. 6** Dimensionless maximum bubble count rate in a cross-section at the downstream end on stepped spillways with embankment dam slopes ( $3.4^\circ \leq \theta \leq 26.6^\circ$ ); comparison of present data (coloured symbols) with previous studies (Table 1, black symbols); Note the different conductivity probe sensor sizes

Despite these limitations, the comparative analysis suggested an increase of  $F_{\max}$  with increasing channel slope for  $\theta \leq 21.8^\circ$  and a slight drop of maximum bubble count rate for  $\theta = 26.6^\circ$ . Further investigations are needed to eliminate effects of different scaling, different conductivity probe sensor size and different downstream distance from the inception point of air entrainment.

The analyses of the air–water interfaces did not only provide information about the number of entrained air bubbles, but also about the air bubble and water droplet chord sizes (Fig. 7). The chord sizes did not represent the exact sizes of the particles, but were a characteristic indicator for the air–water interfaces. The probability analyses of the air–water interfaces showed that most air bubble and water droplet chords had a lengths scale of about 1 to 3 mm for all stepped spillways. All probability distribution functions of the chord sizes followed log-normal correlations (Fig. 7). The comparison of the bubble and droplet chord sizes for stepped spillways with different slopes might show an effect of the channel slope upon the chord sizes. The recording of the air–water interfaces is affected by the probe tip diameter and the comparison of the present stepped spillways with  $\theta = 8.9^\circ$  and  $\theta = 26.6^\circ$  was not possible.

## 5 Re-oxygenation rate

The calculation of the aeration efficiency was based upon oxygen to allow a comparison with direct dissolved oxygen measurements on stepped spillways by [2,3,29]. The significant concentration of nitrogen in the atmosphere was neglected herein, but comparative analyses showed little effect upon the aeration efficiency.

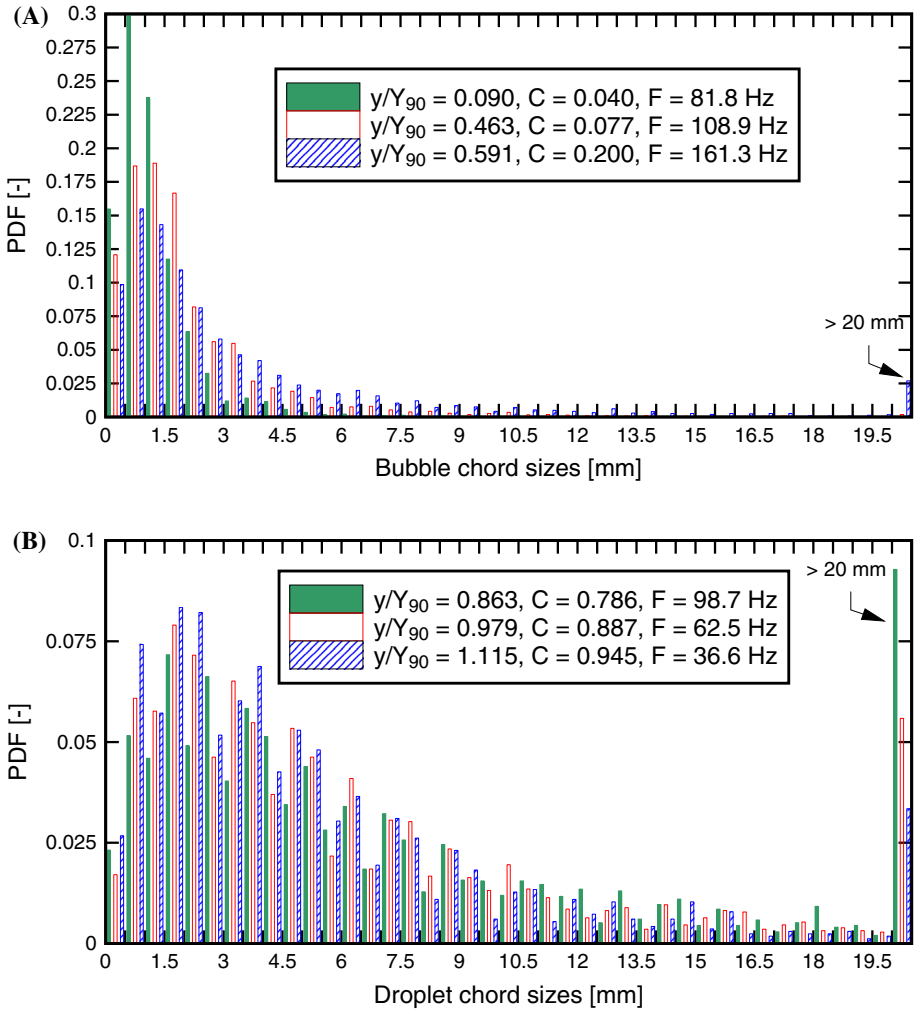


**Fig. 7** Probability distribution functions of air bubble and water droplet chord sizes on flat stepped spillway ( $\theta = 26.6^\circ$ ,  $h = 10\text{ cm}$ ). **a** Air bubble chord sizes:  $d_c/h = 1.29$ ,  $q_w = 0.144\text{ m}^2/\text{s}$ ,  $Re = 5.7 \times 10^5$ . **b** Water droplet chord sizes:  $d_c/h = 1.49$ ,  $q_w = 0.180\text{ m}^2/\text{s}$ ,  $Re = 7.2 \times 10^5$

For all present experiments, the aeration efficiency was calculated based upon air–water flow measurements. The aeration efficiency  $E(O_2)$  was calculated with Eq. (5) and further experimental data were reanalysed (Table 1). The present data are illustrated with colored symbol in Fig. 8 in dimensionless terms per meter drop in invert elevation  $\Delta z_o$  as a function of the dimensionless rate of energy dissipation  $\Delta H/H_{max}$ . In Fig. 8, further data are also added as well as the dissolved oxygen (DO) measurements by [3,29].

All data were in relatively close agreement with slight variations linked with different conductivity probe sensor sizes, different channel slope and stepped configurations. All data showed a monotonic increase of aeration efficiency with increasing rate of energy dissipation. The relationship was best correlated by a power law for all data based upon conductivity probe and dissolved oxygen measurements:

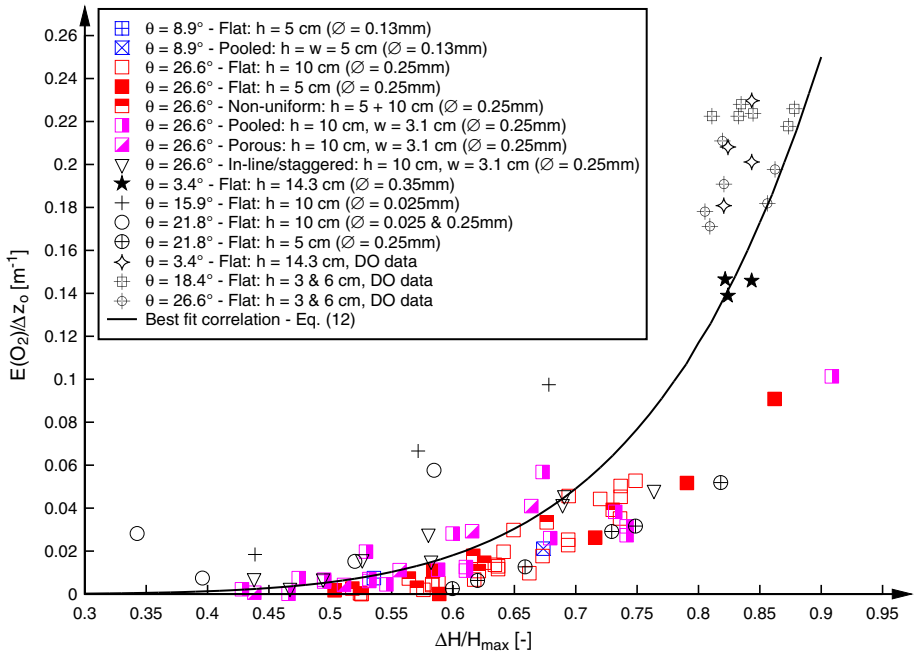


**Fig. 8** Aeration efficiency per meter drop in invert elevation  $E(O_2)/\Delta z_0$  in terms of dissolved oxygen at 20° Celsius at the downstream end of the stepped chute; comparison of present data (coloured symbols) with previous data with embankment dam slopes ( $3.4^\circ \leq \theta \leq 26.6^\circ$ ); Comparison between dissolved oxygen (DO) measurements, the integration of the mass transfer Eq. (6) and best fit correlation (Eq. (12)); Note the different conductivity probe sensor sizes

$$\frac{E(O_2)}{\Delta z_0} = 0.495 \times \left( \frac{\Delta H}{H_{max}} \right)^{6.48} \quad R = 0.87 \quad (12)$$

The present findings confirmed the results of [14] who linked the aeration rate of the flow to the energy dissipation. The air–water flows were highly turbulent with strong interactions between different regions of the flow including the cavity recirculations, the intermediate flow region and the free-surface aeration. The present findings indicated that a large proportion of the kinetic energy was dissipated in the flow region with strong air–water interactions within the intermediate flow region ( $0.3 < C < 0.7$ ). This flow region was characterised by large numbers of entrained air bubbles, largest numbers of interface areas and strong turbulence levels. The results highlight the important role of the intermediate flow region for the energy dissipation and for the aeration efficiency.

The direct dissolved oxygen measurements by [3,29] are consistent with prototype dissolved oxygen measurements of stepped cascades [7]. Hence, the dissolved oxygen data are reference values for the conductivity probe measurements. The present results show the possibility to use conductivity probe measurements for the quantification of the re-oxygenation performance. Differences exist between the conductivity and the direct dissolved oxygen measurements which might be linked with the conductivity sensor size limiting the size of the minimum detectable air bubble chords, the interfacial area and hence the aeration efficiency. Even though a close agreement was observed in terms of aeration efficiencies for the conductivity probe data independently of channel slope ( $3.4^\circ \leq \theta \leq 26.6^\circ$ ), some data

scatter existed (Fig. 8). Small differences in both aeration efficiency and energy dissipation rate were observed for the different stepped configurations of the present study which was linked with variations in flow patterns and air–water flow properties between flat and pooled stepped configurations [13, 17]. Overall, the present results confirm the strong re-oxygenation rates on stepped spillways.

## 6 Conclusion

Stepped spillway flows are strongly aerated downstream of the inception point of free-surface aeration and a complex mixture of air–water interfaces exists. The number of air bubbles per unit time and the specific interfacial area increase along the stepped chute without reaching uniform equilibrium conditions. The aeration is significant for re-oxygenation applications and the identification of an optimum stepped spillway design for typical embankment dam slopes ( $3.4^\circ \leq \theta \leq 26.6^\circ$ ) is relevant in terms of aeration and air–water mass transfer. Herein air–water flow experiments were conducted on several stepped spillway models with  $\theta = 8.9^\circ$  and  $26.6^\circ$ . The aeration, energy dissipation and re-oxygenation efficiencies were calculated based upon detailed phase-detection probe measurements. The present data were compared with previous stepped spillway studies comprising both phase-detection probe data and direct dissolved oxygen measurements.

The results highlighted the strong energy dissipation performances for all stepped chutes linked with the air–water interfaces. The significant flow aeration was shown by the depth averaged air concentration at the downstream end of the chutes which was significantly larger for slopes  $3.4^\circ \leq \theta \leq 21.8^\circ$  compared to smooth spillway data and equilibrium air concentrations for smooth chutes, but lower for  $\theta = 26.6^\circ$ . The maximum bubble count rate in a cross-section increased with increasing channel slope reaching a maximum for the slope with  $\theta = 21.8^\circ$ . Within the range of embankment dam sloped chutes ( $3.4^\circ \leq \theta \leq 26.6^\circ$ ) and for skimming flow discharges, a stepped chute slope of  $\theta = 21.8^\circ$  appeared optimum for aeration performances. The re-oxygenation rate was calculated based upon conductivity probe data highlighting significant flow aeration independently of channel slope, stepped chute configuration and conductivity sensor size. The present data were compared with re-analysed phase-detection probe data and direct dissolved oxygen measurements on stepped chutes. All data were in good agreement, showing a parabolic increase of aeration efficiency per unit drop in elevation with increasing energy dissipation rate. The findings highlighted the relevance of the intermediate flow region ( $0.3 < C < 0.7$ ) for both re-aeration performance and energy dissipation.

**Acknowledgments** The authors acknowledge the financial support of the Australian Research Council (Grants DP0878922 and DPDP120100481).

## References

1. Boes RM (2000) Zweiphasenströmung und Energieumsetzung an Grosskaskaden, PhD thesis, VAW-ETH, Zürich, Switzerland (in German)
2. Bung DB (2009) Zur selbstbelüfteten Gerinneströmung auf Kaskaden mit gemäßigter Neigung. PhD Thesis, Lehr- und Forschungsgebiet Wasserwirtschaft und Wasserbau, Bergische Universität Wuppertal, Germany (in German)
3. Bung DB, Schlenkhoff A (2009) Prediction of oxygen transfer in self-aerated skimming flow on embankment stepped spillways, 33rd IAHR World Congress, Vancouver, Canada

4. Carosi G, Chanson H (2006) Air-water time and length scales in skimming flow on a stepped spillway. Application to the spray characterisation. Report No. CH59/06, Division of Civil Engineering, The University of Queensland, Brisbane, Australia, July
5. Chanson H (1997a) Air bubble entrainment in open channels. Flow structure and bubble size distributions. *Int J Multiph Flow* 23(1):193–203
6. Chanson H (1997b) Measuring air–water interface area in supercritical open channel flow. *Water Res* 31(6):1414–1420
7. Chanson H (2001) The hydraulics of stepped chutes and spillways. Balkema, Lisse, p 418
8. Chanson H (2002) Air–water flow measurements with intrusive phase-detection probes. Can we improve their interpretation? *J Hydraul Eng ASCE* 128(3):252–255
9. Chanson H (2006) Minimum specific energy and critical flow conditions in open channels. *J Irrig Drain Eng ASCE* 132(5):498–502
10. Chanson H, Carosi G (2007) Advanced post-processing and correlation analyses in high-velocity air–water flows. *Environ Fluid Mech* 7(6):495–508
11. Chanson H, Toombes L (2002a) Air–water flows down stepped chutes: turbulence and flow structure observations. *Int J Multiph Flow* 28(11):1737–1761
12. Chanson H, Toombes L (2002b) Energy dissipation and air entrainment in stepped storm waterway: experimental study. *J Irrig Drain Eng ASCE* 128(5):305–315
13. Felder S (2013) Air–water flow properties on stepped spillways for embankment dams: aeration, energy dissipation and turbulence on uniform, non-uniform and pooled stepped chutes. PhD Thesis, The University of Queensland, Australia
14. Felder S, Chanson H (2009a) Energy dissipation, flow resistance and gas-liquid interfacial area in skimming flows on moderate-slope stepped spillways. *Environ Fluid Mech* 9(4):427–441
15. Felder S, Chanson H (2009b) Turbulence, dynamic similarity and scale effects in high-velocity free-surface flows above a stepped chute. *Exp Fluids* 47(1):1–18
16. Felder S, Chanson H (2011) Air–water flow properties in step cavity down a stepped chute. *Int J Multiph Flow* 37(7):732–745
17. Felder S, Chanson H (2013) Aeration, flow instabilities, and residual energy on pooled stepped spillways of embankment dams. *J Irrig Drain Eng ASCE* 139(10):880–887
18. Ferrell RT, Himmelblau DM (1967) Diffusion coefficients of nitrogen and oxygen in water. *J Chem Eng Data* 12(1):111–115
19. Gonzalez CA (2005) An experimental study of free-surface aeration on embankment stepped chutes. PhD Thesis, Department of Civil Engineering, The University of Queensland, Brisbane, Australia
20. Guenther P, Felder S, Chanson H (2013) Flow aeration, cavity processes and energy dissipation on flat and pooled stepped spillways for embankments. *Environ Fluid Mech* 13(5):503–525
21. Gulliver JS (1990) Introduction to air–water mass transfer. In: Proceedings of 2nd international symposium on gas transfer at water surfaces, air–water mass transfer; ASCE Publ., Minneapolis MN, pp 1–7
22. Kawase Y, Moo-Young M (1992) Correlations for liquid-phase mass transfer coefficients in bubble column reactors with newtonian and non-newtonian fluids. *Can J Chem Eng* 70:48–54
23. Matos J (1999) Air entrainment and energy dissipation on stepped spillways. PhD Thesis, Technical University of Lisbon, Portugal
24. Meireles I, Matos J (2009) Skimming flow in the nonaerated region of stepped spillways over embankment dams. *J Hydraul Eng ASCE* 135(8):685–689
25. Ohtsu I, Yasuda Y, Takahashi M (2004) Flow characteristics of skimming flows in stepped channels. *J Hydraul Eng ASCE* 130(9):860–869
26. Straub LG, Anderson AG (1958) Experiments on self-aerated flow in open channels. *J Hydraul Div ASCE* 84(HY7):1–35 paper 1890
27. Thorwarth J (2008) Hydraulisches Verhalten der Treppengerinne mit eingetieften Stufen - Selbstinduzierte Abflusstationaritäten und Energiedissipation. PhD Thesis, University of Aachen, Germany (in German)
28. Toombes L (2002) Experimental study of air–water flow properties on low-gradient stepped cascades. PhD Thesis, Dept. of Civil Engineering, University of Queensland, Australia
29. Toombes L, Chanson H (2005) Air–water mass transfer on a stepped waterway. *J Environ Eng ASCE* 131(10):1377–1386
30. Wood I (1983) Uniform region of self-aerated flow. *J Hydraul Eng* 109(3):447–461